Mathematical Biosciences and Engineering

MBE, 19 (2): 1891–1908.
DOI: 10.3934/mbe.2022089
Received: 24 October 2021
Accepted: 14 December 2021
Published: 20 December 2021

http://www.aimspress.com/journal/MBE

*Research article*

# Brain tissue segmentation via non-local fuzzy c-means clustering combined with Markov random field

**Jianhua Song[1,2,*] and Lei Yuan[2]**

[1] The Key Laboratory of Intelligent Optimization and Information Processing, Minnan Normal University, Zhangzhou, 363000, China
[2] College of Physics and Information Engineering, Minnan Normal University, Zhangzhou, 363000, China

*** Correspondence:** Email: songjianhua@mnnu.edu.cn; Tel: +8605962591443.

**Abstract:** The segmentation and extraction of brain tissue in magnetic resonance imaging (MRI) is a meaningful task because it provides a diagnosis and treatment basis for observing brain tissue development, delineating lesions, and planning surgery. However, MRI images are often damaged by factors such as noise, low contrast and intensity brightness, which seriously affect the accuracy of segmentation. A non-local fuzzy c-means clustering framework incorporating the Markov random field for brain tissue segmentation is proposed in this paper. Firstly, according to the statistical characteristics that MRF can effectively describe the local spatial correlation of an image, a new distance metric with neighborhood constraints is constructed by combining probabilistic statistical information. Secondly, a non-local regularization term is integrated into the objective function to utilize the global structure feature of the image, so that both the local and global information of the image can be taken into account. In addition, a linear model of inhomogeneous intensity is also built to estimate the bias field in brain MRI, which has achieved the goal of overcoming the intensity inhomogeneity. The proposed model fully considers the randomness and fuzziness in the image segmentation problem, and obtains the prior knowledge of the image reasonably, which reduces the influence of low contrast in the MRI images. Then the experimental results demonstrate that the proposed method can eliminate the noise and intensity inhomogeneity of the MRI image and effectively improve the image segmentation accuracy.

**Keywords:** Magnetic resonance imaging; brain tissue segmentation; fuzzy c-means clustering; Markov random field; non-local constraints

## 1. Introduction

In the clinical diagnosis and treatment, to analyze the brain development and describe the lesion, it is necessary to segment the brain magnetic resonance imaging (MRI) accurately, so as to provide the necessary support for further treatment plan [1–3]. However, during the image acquisition process, affected by the performance of the imaging device, the inhomogeneity of radio field (RF) intensity and postural change of the patients, there are many problems in MRI image, such as noise, intensity distribution heterogeneity (also known as bias field) and low contrast, which cause some interference in the process of brain tissue segmentation [4,5].

Fuzzy c-means clustering (FCM) is a data partition method based on fuzzy set theory. As one of the machine learning algorithms, FCM has become an effective means of image segmentation [6–8], and its success is attributed to its fuzzy nature, which can get more image features from the image. However, the FCM usually performs well on noise-free images, when the image to be processed is disturbed by noise, inhomogeneous intensity or artifacts, the segmentation result is not satisfactory. Since only the non-robust Euclidean distance is used as the similarity metric in the objective function of the FCM, the similarity between neighboring pixels in the image is neglected. To this end, many scholars have proposed different improvement schemes. Pham et al. proposed a robust fuzzy c-means (R-FCM) model [9], which introduces a local spatial regularization term in the objective function to eliminate the improbable classification results of pixels in images. Cui et al. [10] designed a model of fuzzy energy minimization. Firstly, the objective function of local FCM clustering around each center pixels is defined. Then, the objective function is combined with the center pixel of the neighborhood to construct global fuzzy energy, and the results are obtained by minimizing the energy function. Although the aforementioned methods overcome the influence of noise to some extent, the image details and edge processing effect are not satisfactory. Markov random field (MRF) has been widely used as a spatially constrained probability statistical model [11–13]. For images, MRF can fully consider the relationship between pixels in the spatial domain and effectively describe the neighborhood of an image. Chen et al. [14] proposed a modified FCM method by integrating the advantages of fuzzy clustering and the hidden MRF, the novel clustering algorithm has a special ability to incorporate spatial information by using a random field model and meanwhile overcomes the disadvantages of noise sensitivity of the traditional FCM algorithms. This algorithm is named FCMRF, and it has good immunity against noise and artifacts. However, it also increases the computational complexity of implementation procedures.

In this paper, a non-local FCM algorithm combined with Markov random field (NL-FCMRF) for brain tissue segmentation is proposed. To eliminate the interference of noise in MRI images, a non-local regularization item is integrated into the fuzzy c-means clustering, at the same time, we also utilize local spatial correlation of MRF to enhance the robustness to noise, and then the linear model of bias field is fused into the objective function to realize effective estimation of intensity inhomogeneity.

The remainder of this paper is arranged as follows. Section 2 introduces the work related to our algorithm. The rationale of the proposed NL-FCMRF algorithm is described in detail in Section 3. The experimental results of NL-FCMRF with the state-of-the-art models and qualitative and quantitative comparison and evaluation are demonstrated in Section 4. Finally, a conclusion is summarized in Section 5.

## 2. Related works

### *2.1. Markov radom field*

Let Z={$Z_1$, $Z_2$, ⋯, $Z_n$} be a family of random variables defined in set $S$, in which each random variable $Z_i$ takes a value $z_i$ in Λ, $z_i$ is called a realization of $Z_i$, Λ denotes the configuration space of $z_i$, and the random variable family $Z$ can be regarded as a random field. $N_i$ denotes the neighborhood set of $z_i$ and satisfies $N_i \subset S$. Let the probability of $Z_i$ taking the value $z_i$ can be expressed as $P(Z_i=z_i)$, abbreviated $P(z_i)$, and the joint probability can be expressed $P(Z=z)=P(Z_1=z_1, \cdots, Z_n=z_n)$ and abbreviated $P(z)$. Let neighborhood set of the position of a site $i$ is $N_i$, if the random field $Z$ can satisfy the following two conditions:

$$P(z) > 0, \ \forall z \in \Lambda \tag{1}$$

$$P\left(z_i \middle| z_{(i)}\right) = P\left(z_i \middle| z_{N_i}\right), \quad \forall z \in \Lambda, \ i \in S \tag{2}$$

The random field $Z$ is a Markov random field [15], where $z_{(i)}$ denotes all the pixels except $z_i$ in the image, and $z_{Ni}$ denotes the pixels in the neighborhood set. The conditional probability in Eq (2) is limited by the consistency condition in the process of solving, so it is difficult to solve. Fortunately, Hammersley and Clifford proposed the Hammersley-Clifford theorem and pointed out the equivalence between MRF and Gibbs distribution [16]. Therefore, a joint probability method for dealing with specified MRF is provided in mathematics.

Gibbs distribution is a representation of the joint probability in configuration space Λ, which can be defined by a set of potential functions $V=\{V_C, C \subset S\}$. Let the energy function associated with a particular implementation of the random field be defined as

$$U(z) = -\sum_{C \subset S} V_C(z) \tag{3}$$

Joint probability density $P(z)$ can be written as

$$P(z) = \frac{1}{W} exp\left\{-\frac{1}{T} U(z)\right\} \tag{4}$$

where $T$ is a temperature constant, generally set to 1, $W$ is a standardized constant called partition function, its expression is

$$W = \sum_{z \in \Lambda} exp\left\{-\frac{1}{T} U(z)\right\} \tag{5}$$

Energy function $U(z)$ can be written by using first-order and second-order neighborhoods

$$U(z) = \sum_{\{i\} \in C_1} V_1(z_i) + \sum_{\{i, \ j\} \in C_2} V_2(z_i, \ z_j) \tag{6}$$

Using the properties of the Gaussian Markov random field (GMRF) model [17], the local conditional probability $P(z_i|z_{N_i})$ can be written as

$$P(z_i|z_{N_i}) = \frac{e^{-\left[V_1(z_i) + \sum_{j \in N_i} V_2(z_i, \ z_j)\right]}}{\sum_{z_i \in \Lambda} e^{-\left[V_1(z_i) + \sum_{j \in N_i} V_2(z_i, \ z_j)\right]}} \tag{7}$$

Potts model is the most widely used model in the case of multi-label [18], which can prevent the edges of objects from being over-smoothed. Generally, Potts model only considers the binary potential function in the form of

$$V_2(z_i,\ z_j) = \begin{cases} 0, & z_i = z_j \\ \alpha, & z_i \neq z_j \end{cases} \tag{8}$$

where $\alpha$ is the corresponding clique potential parameter. The local probability of the Potts model is

$$P(z_i|z_{N_i}) = \frac{e^{-[\alpha n_i(z_i)]}}{\sum_{z_i \in \Lambda} e^{-[\alpha n_i(z_i)]}} \tag{9}$$

where $n_i(z_i)$ denotes the number of neighboring sites of elements that are not equal to $z_i$ in the neighborhood set of the position of a site $i$.

Based on the former research, Ribes et al. proposed a framework for automatic segmentation of breast MRI images [19]. Firstly, the image is preprocessed by anisotropic filtering and then segmented by the MRF model. All parameters can be updated automatically, and the partial volume effect problem in MRI images is solved to some extent. However, the image is smoothed, and some important edge information is easy to be ignored because of the filtering preprocessing.

### *2.2. Fuzzy c-means clustering*

FCM is a data classification method proposed by Dunn [20] and developed by Bezdek [21]. This algorithm partitions unlabeled data samples by the objective function based on some norm and clustering prototype. Let $X = \{x_1, x_2, \cdots, x_N\} \subset R^c$ denotes a given sample set, which is the grayscale set of each pixel in an image. $c$($c$>1) is the dimension of sample space, $N$ is the number of image pixels. $c$ is the number of clusters that partition $X$. FCM calculates the fuzzy membership matrix $U = \{u_{ki}\}$ satisfying the following constraints:

$$\sum_{k=1}^{c} u_{ki} = 1, \quad \sum_{i=1}^{N} u_{ki} > 0, \quad 1 \le k \le c,\ 1 \le i \le N \tag{10}$$

$$u_{ki} \in [0,1], \quad 1 \le k \le c, \quad 1 \le i \le N \tag{11}$$

The objective function of FCM is

$$J_{FCM}(U,V) = \sum_{k=1}^{c} \sum_{i=1}^{N} u_{ki}^m\, d_{ki}^2 \tag{12}$$

In Eq (12), $m$ ($m$>1) is called fuzzy index, $U$=$\{u_{ki}\}$ is a matrix called fuzzy membership matrix, where $u_{ki}$ is the fuzzy membership of pixel $x_i$, $V = \{v_1, v_2, \cdots, v_N\}$ is a $N \times c$ matrix composed of $c$ clustering center vectors, $d_{ki} = \|x_i - v_k\|$ denotes the distance measure from the pixel $x_i$ to the cluster center $v_k$. There are many ways to express distance measure, and the most used measure is Euclidean distance. Next, the extreme value of the objective function $J_{FCM}$ is obtained by the Lagrange multiplier method, which leads to Eqs. (13) and (14).

$$v_k = \frac{\sum_{i=1}^{N} u_{ki}^m x_i}{\sum_{i=1}^{N} u_{ki}^m}, \qquad 1 \le k \le c \tag{13}$$

$$u_{ki} = \frac{1}{\sum_{l=1}^{c} \left(\frac{d_{ki}}{d_{li}}\right)^{\frac{2}{m-1}}}, \quad 1 \le k \le c, \quad 1 \le i \le N \tag{14}$$

## 3. Non-local fuzzy c-means clustering combined with MRF

MRF is used to state the spatial constraints between local pixels of an image, and then the image is segmented by the maximum a posterior (MAP) criterion. This is one of the better methods to achieve effective segmentation of texture images [22–24]. However, the method has the problem of "hard partition" as deciding the classifications of pixels. For these problems such as noise, overlapping regions and low contrast in medical images, MRF seems to be inadequate. Therefore, the fusion of fuzzy theory (soft partition) and MRF theory and comprehensive utilization of the advantages of the two methods can significantly improve the accuracy of segmentation and overcome noise interference and low contrast in MRI images [25,26].

### *3.1. Distance measure fused MRF*

In FCM, distance measure $d_{ki}$ plays an important role in evaluating the difference between different sample points and the cluster center. However, $d_{ki}$ only uses the grayscale distance between pixels without involving the influence of spatial distance between pixels. Therefore, we study the improvement strategy combined Eq (9) for $d_{ki}$ and design a new distance measure $D_{ki}$, as shown in Eq (15).

$$D_{ki} = \frac{d_{ki}}{sqrt\left(P(z_i=k|z_{N_i})\right)} \tag{15}$$

where $d_{ki}$ is the Euclidean distance, $z_{Ni}$ denotes the coordinate label of the neighborhood set of the site $i$, and $P(z_i = k|z_{Ni})$ denotes the prior probability that the pixel point belongs to the $k$-th cluster under the condition that the neighborhood site label is known. The new distance measure $D_{ki}$ includes both gray-scale distance between pixels and the influence of the classification label of local neighborhood pixel on the objective pixel classification. In terms of an image, the gray-scale correlation between local neighboring pixels is generally high. If the probability of the neighboring pixels being labeled as the $k$-th cluster is high, the probability of the objective pixel being labeled as the $k$-th cluster also increases, and it is inversely proportional to the spatial distance $d_{ki}$. The prior probability $P(z_i=k|z_{Ni})$ can be calculated using Potts model of MRF, and the formula is as follows:

$$P(z_i|z_{N_i}) = \frac{e^{-\gamma \sum_{j\in N_i}\delta(z_i,z_j)}}{\sum_{z_i\in\Lambda} e^{-\gamma \sum_{j\in N_i}\delta(z_i,z_j)}} \tag{16}$$

where $\delta(z_i, z_j) = \begin{cases} 1, & z_i = z_j \\ 0, & otherwise \end{cases}$, $\gamma$ is the clique potential parameter.

### *3.2. Non-local framework*

Potts model is introduced into distance measure, and image neighborhood information is considered, which can improve the robustness of FCM clustering. In brain MR images, the neighborhood structure of one pixel may appear similarly in the neighborhood of other pixels of the same image. To use the global structure information of the image [27,28], non-local constraints can be added to the model. Therefore, a weighted measure $S_{ij}$ is introduced and its expression is

$$S_{ij} = \frac{1}{E_i} e^{\left(\frac{-\left\|x(N_i)-x(N_j)\right\|_{2,\sigma}^2}{h}\right)} \tag{17}$$

where $h$ is a constant proportional to the noise variance, which adjusts the attenuation degree of the similar measure $S_{ij}$ and satisfies $0<S_{ij}<1$ and $\sum_{j\in w_i^u} S_{ij} = 1$. $W_i^u$ is a search window with radius $u$ around $x_i$, $x(N_i)$ and $x(N_j)$ denote the gray-scale vectors in neighborhood window $N_i$ and $N_j$ of radius $s$ around $x_i$ and $x_j$, respectively. $\left\|x(N_i) - x(N_j)\right\|_{2,\sigma}^2$ is a 2-norm representing the distance between $x(N_i)$ and $x(N_j)$. $E_i$ is a normalized constant and its expression is

$$E_i = \sum_{j\in w_i^u} e^{\left(\frac{-\left\|x(N_i)-x(N_j)\right\|_{2,\sigma}^2}{h}\right)} \tag{18}$$

$S_{ij}$ is a weighted Gaussian distance. This factor can utilize the global structure information of the image without any prior knowledge, and it is very helpful for the label classification of pixels. Based on R-FCM algorithm, an energy function combined Markov random field with non-local constraints is designed (called NL-FCMRF). The energy function is

$$J_m = \sum_{k=1}^{c}\sum_{i=1}^{N} u_{ki}^m D_{ki}^2 + \frac{\beta}{2}\sum_{k=1}^{c}\sum_{i=1}^{N} u_{ki}^m \sum_{j\in w_i^u} S_{ij} \sum_{l\in L_k} u_{jl}^m \tag{19}$$

where $\beta$ is an adjustment factor, and it controls the balance between the former term and the non-local regular term in the energy function. The value of $\beta$ can be set by the cross-validation method [9].

Combined with the constraint $\sum_{i=1}^{c} u_{ki} = 1$, $0 \le u_{ki} \le 1$and $m$>1, according to Lagrange's optimal criterion, let

$$L(u_{ki}, v_k, \lambda_i, \beta) = \sum_{k=1}^{c}\sum_{i=1}^{N} u_{ki}^m D_{ki}^2 + \frac{\beta}{2}\sum_{k=1}^{c}\sum_{i=1}^{N} u_{ki}^m \sum_{j\in w_i^u} S_{ij} \sum_{l\in L_k} u_{jl}^m + \sum_{i=1}^{N}\lambda_i(1 - \sum_{k=1}^{c} u_{ki}) \tag{20}$$

Calculating the partial derivatives of Eq (20) with respect to $u_{ki}$ and $\lambda_i$, respectively, and let $\frac{\partial L}{\partial u_{ki}} = 0$ and $\frac{\partial L}{\partial \lambda_i} = 0$, as shown in Eqs. (21) and (22).

$$\frac{\partial L}{\partial u_{ki}} = m u_{ki}^{m-1}\left(D_{ki}^2 + \beta \sum_{j\in w_i^u} S_{ij} \sum_{l\in L_k} u_{jl}^m\right) - \lambda_i = 0 \tag{21}$$

$$\frac{\partial L}{\partial \lambda_i} = 1 - \sum_{k=1}^{c} u_{ki} = 0 \tag{22}$$

where the factor of 1/2 on $\beta$ vanishes because the partial derivative operation results in a product term of $u_{ki}$ and its neighbors, plus a reverse product term of the neighbors and $u_{ki}$. Setting this partial derivative to zero can be obtained from Eq (21).

$$u_{ki} = \left(\frac{\lambda_i}{m\left(D_{ki}^2 + \beta \sum_{j\in w_i^u} S_{ij} \sum_{l\in L_k} u_{jl}^m\right)}\right)^{1/(m-1)} \tag{23}$$

Bring Eq (23) into Eq (22), yielding

$$\left(\frac{\lambda_i}{m}\right)^{-1/(m-1)} = \frac{1}{\sum_{k=1}^{c}\left(D_{ki}^2+\beta\sum_{j\in w_i^u} S_{ij}\sum_{l\in L_k} u_{jl}^m\right)^{-1/(m-1)}} \tag{24}$$

Bring Eq (24) into Eq (23), yielding

$$u_{ki} = \frac{\left(D_{ki}^2+\beta\sum_{j\in w_i^u} S_{ij}\sum_{l\in L_k} u_{jl}^m\right)^{-1/(m-1)}}{\sum_{t=1}^{c}\left(D_{ti}^2+\beta\sum_{j\in w_i^u} S_{tj}\sum_{l\in L_k} u_{jl}^m\right)^{-1/(m-1)}} \tag{25}$$

Similarly, computing the partial derivative of $L$ about $v_k$ and setting $\partial L/\partial v_k = 0$ yields

$$\frac{\partial L}{\partial v_k} = \sum_{i=1}^{N}\left(\frac{u_{ki}^m}{P(z_i=k|z_{N_i})}\right)(x_i - v_k) = 0 \tag{26}$$

Obtained from Eq (26)

$$v_k = \frac{\sum_{i=1}^{N}\left(\frac{u_{ki}^m}{P(z_i=k|z_{N_i})}\right)x_i}{\sum_{i=1}^{N}\frac{u_{ki}^m}{P(z_i=k|z_{N_i})}} \tag{27}$$

### *3.3. The implementation of NL-FCMRF*

The detailed implementation steps of the NL-FCMRF is as shown in Table 1.

**Table 1.** The pseudo code of NL-FCMRF.

**Algorithm 1** NL-FCMRF

**Begin**

**Input:**

the brain MRI images

**Initialization:**

number of cluster $c$=4, fuzzy coefficient $m$=2 and parameters $u$=8;

iterations number $t$ =0 and stop iteration $\varepsilon$=0.001;

cluster prototype $V^{(1)}$ and fuzzy membership $u_{ki}^{(0)}$ randomly

**Process:**

compute the prior probability $P(z_i=k|z_{Ni})$ and non-local distance measure $S_{ij}$ according to Eqs (16) and (17);

while $|V^{(t+1)} - V^{(t)}| < \varepsilon$

update fuzzy membership degree $u_{ki}^{(t)}$;

update cluster prototype $V^{(t)}$;

$t$= $t$+1

**Output:**

segmentation results

**End**

## 4. Experimental results and analysis

Two types of brain MRI images are selected as experimental samples: one is the T1-weighted synthetic brain MRI images acquired from the Brainweb [29], and the other is the real brain MRI image acquired from the IBSR (Internet Brain Segmentation Repository) [30]. In the experiments, the tested samples are divided into four parts: white matter (WM), gray matter (GM), cerebrospinal fluid (CSF) and background. The computer configuration when all experiments are implemented is as follows: Core i5-7300 CPU, 4GB RAM, the corresponding operating system is Windows 10, and the programming software is MATLAB 2015b.

### *4.1. Results on synthetic brain MRI image*

BrainWeb is a brain MRI image database, which provides synthetic brain MRI data with different modes and parameters including T1-weighted, T2-weighted and proton density (PD) images. The 3D image slice has an anatomical ground truth, and the database also provides the classification label for each intracranial voxel. In the experiments, T1-weighted images with 1 mm slice thickness are used, and the 2D images are acquired from 3D images sliced by three directions: axial, sagittal and coronal, respectively. Before segmentation, the unnecessary cranial tissues were removed. Markov random field adopts a second-order neighborhood system, and the search radius of non-local constraints is $u = 8$.

#### 4.1.1. Image segmentation of noisy brain MRI

Firstly, four groups of brain MRI slice images with 9% noise are selected and they are extracted from axial slice images indexed to 45, 60, 93 and 113. These images have been preprocessed and the skull, muscle and blood vessels are removed. The segmentation results of standard FCM, R-FCM [9], MICO [31], ARKFCM [32], FCMRF [14] and NL-FCMRF are compared under the same experimental conditions, as shown in Figure 1.

In Figure 1, the first column is a group of noisy 2D sliced images with 9% noise level, the second column is the ground truth, and columns 3–8 are the experimental results after the implementation of six algorithms. By analyzing the segmentation results in Figure 1, we can get the following conclusions: (1) FCM and MICO are very sensitive to noise. (2) R-FCM can eliminate part of the influence of noise interference, but the segmentation accuracy is not high. (3) Segmentation accuracy of ARKFCM and FCMRF have been greatly improved, however, it is still unsatisfactory for edge and some details of the image. (4) The segmentation results of NL-FCMRF are the closest to ground truth, and the details and edge of the brain tissues are also very clear. In order to show the segmentation results more clearly, the second row of Figure 1 is magnified three times locally, as shown in Figure 2. It can be seen from the local details in Figure 2 (b)–(g) that the NL-FCMRF algorithm can more accurately separate individual brain tissues from noisy images.

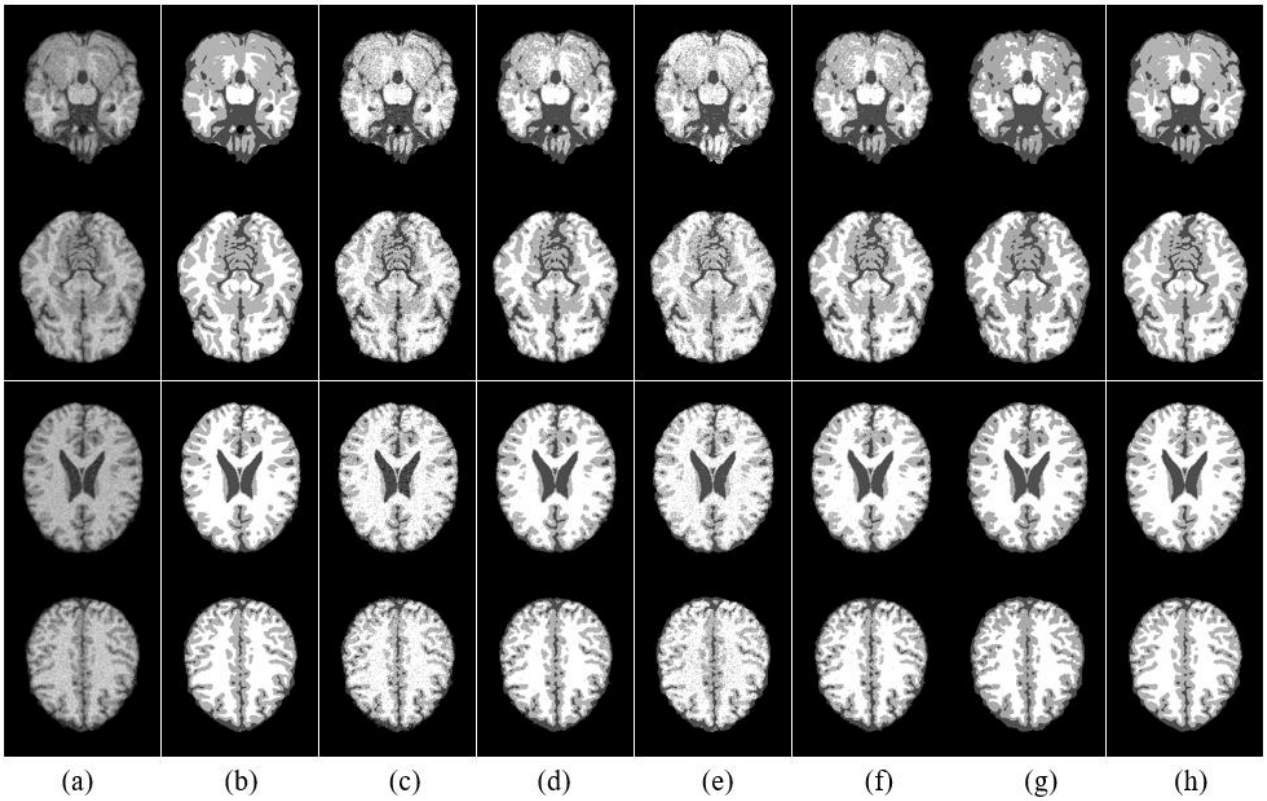


**Figure 1.** The segmentation results by six models for noisy MRI. (a) The original brain MRI slice, (b) ground truth, (c) FCM, (d) R-FCM, (e) MICO, (f) ARKFCM, (g) FCMRF and (h) NL-FCMRF.

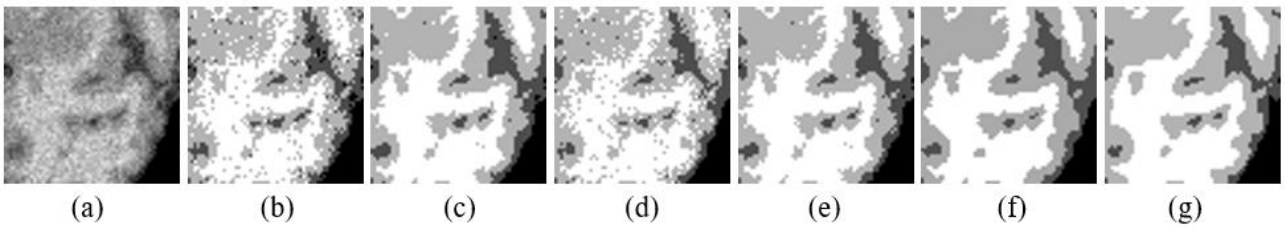


**Figure 2.** The comparison of local enlarged image. (a) Noisy image, (b) FCM, (c) R-FCM, (d) MICO, (e) ARKFCM, (f) FCMRF and (g) NL-FCMRF.

In order to quantitatively evaluate the experimental results, misclassification rate (MCR) is used to compare the performance of the six segmentation methods. The formula for computing MCR is as shown in Eq (28). Eight groups of brain MRI images with different noise levels (from 5% to 35%) are selected and segmented by FCM, R-FCM, MICO, ARKFCM, FCMRF and NL-FCMRF, respectively. The average MCR values of the six methods are counted, and the statistical results are shown in Figure 3.

$$MCR = \frac{Number\ of\ misclassified\ pixels}{Total\ number\ of\ pixels} \tag{28}$$

It can be seen from MCR change curve of WM, GM and CSF segmentation results in Figure 3. As the noise level increases, the MCR of the six algorithms also increases, and the MCR of NL-FCMRF is significantly lower than the other five algorithms. However, when the noise intensity is high, the magnitude of the MCR of all algorithms for images changes slightly. Fortunately, for real brain MRI, the intensity of the noise contained therein will not be as high as 35%.

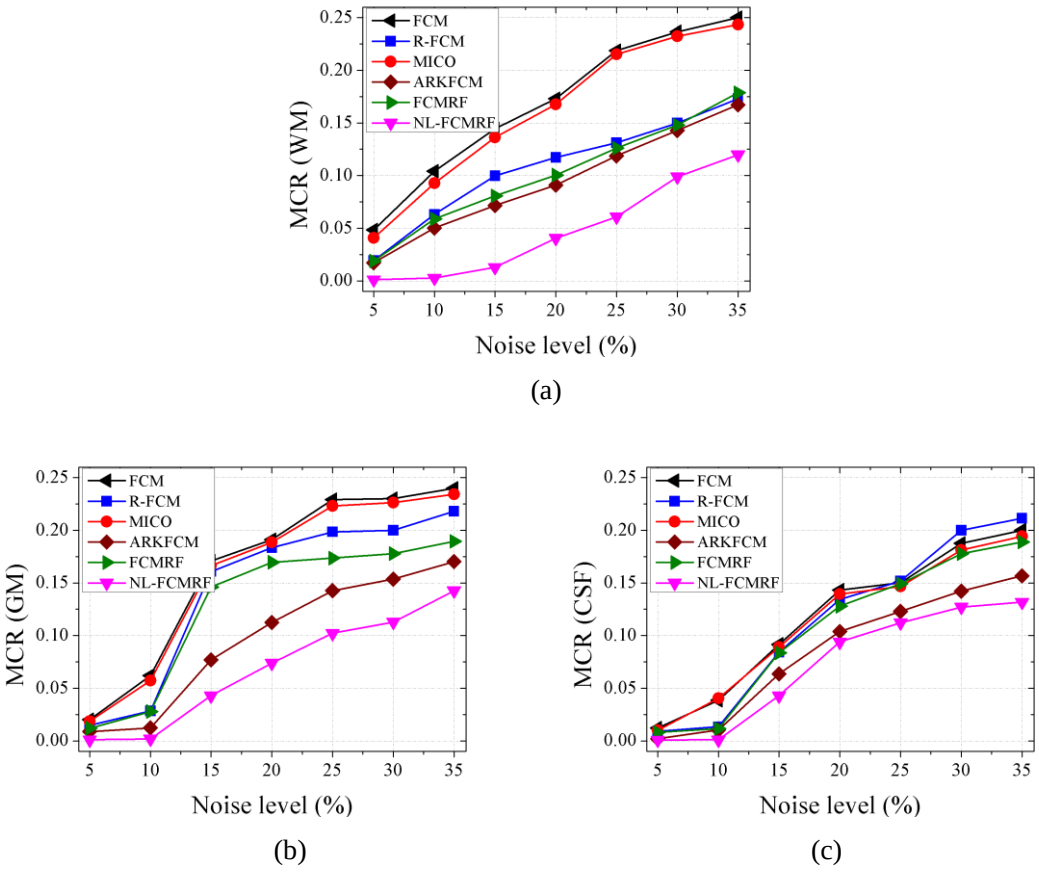


**Figure 3.** MCR values comparison of segmentation results for noisy MR images. (a) MCR values of WM, (b) MCR values of GM and (c) MCR values of CSF.

### 4.1.2. Brain MRI image segmentation of with bias field

In the second experiment, the brain MRI slice images are selected from three different directions, and these images are corrupted by 100% intensity inhomogeneity without noise. A mathematical model can be established to estimate the intensity inhomogeneity according to its smoothly and slowly changing properties [33], and the model is shown in Eq (29).

$$X = bX_0 + N \tag{29}$$

where $X$ denotes the observed image, $X_0$ denotes the corrected image, and $b$ and $N$ denote the bias field and noise existing in the observed image, respectively. An extended objective function can be obtained after taking Eq (29) into Eq (19), as shown in Eq (30).

$$J_m = \sum_{k=1}^{c}\sum_{i=1}^{N} u_{ki}^m \left(\frac{\|x_i - b_i v_k\|^2}{P(z_i=k|z_{N_i})}\right) + \frac{\beta}{2}\sum_{k=1}^{c}\sum_{i=1}^{N} u_{ki}^m \sum_{j\in N_i} S_{ij} \sum_{l\in L_k} u_{jl}^m \tag{30}$$

where $b_i$ is the estimated bias field of the $i$-th pixel. This method assumes that the spatial grayscale of each brain tissue varies independently throughout the image. Therefore, the Lagrange multiplier optimization criterion can be used to estimate $b_i$ in Eq (30), so that the extended NL-FCMRF can eliminate the influence of the bias field, and the experimental results are shown in Figure 4. Column 1 is the observed brain MRI slice images with intensity inhomogeneity, and column 2 to column 7 are the segmentation results of FCM, R-FCM, MICO, ARKFCM, FCMRF and NL-FCMRF, respectively, where FCM, R-FCM, ARKFCM and FCMRF do not consider correcting the bias field, and so these algorithms are difficult to suppress effectively for intensity inhomogeneity because each cluster center is assumed to be stationary in the whole image without effective iterative updates. The MICO algorithm uses a linear combination of a set of basis functions to model the bias field and can achieve high-accuracy bias field estimation when there are enough basis functions. Therefore, the segmentation results of MICO model are hardly affected by intensity inhomogeneity, and can accurately segment each brain tissue. Further, the non-local framework in NL-FCMRF can also greatly improve the segmentation effect of WM, GM and CSF, and update the cluster center effectively.

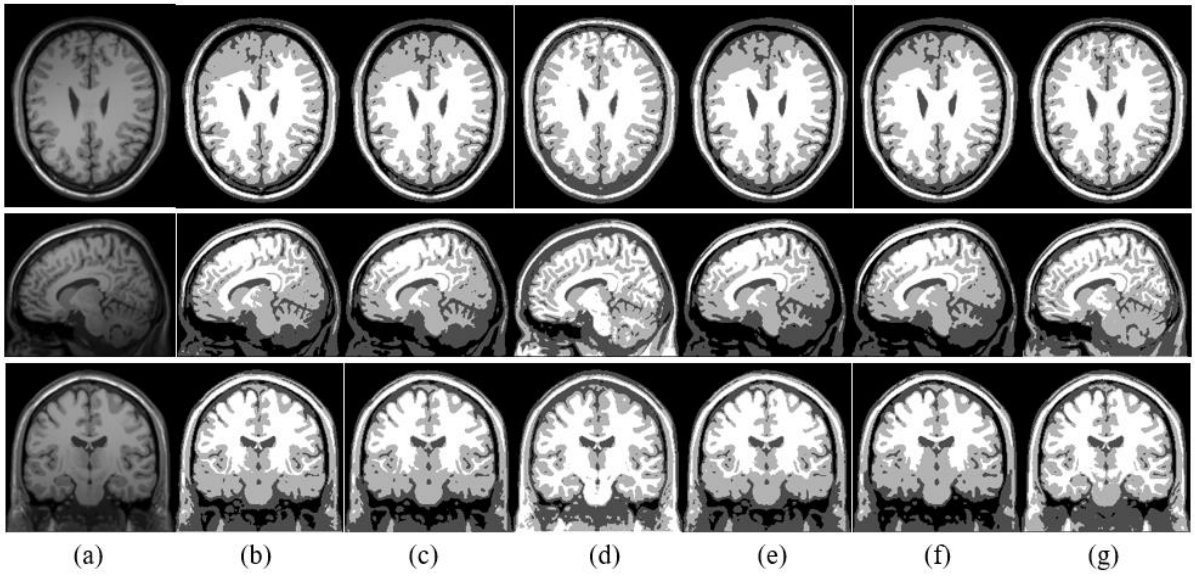


**Figure 4.** The segmentation results for MR images with intensity inhomogeneity. (a) Brain MR slice images, (b) FCM, (c) R-FCM, (d) MICO, (e) ARKFCM, (f) FCMRF and (g) NL-FCMRF.

Similarly, we still use MCR as an objective evaluation index to analyze the performance of six segmentation algorithms, and 12 brain MRI slice images are used as test objects. The MCR values of WM, GM, and CSF are compared when the intensity inhomogeneity level varied from 10% to 90% for the MRI slices with free noise, and the various curves of MCR values are drawn in Figure 5. It can be seen from Figure 5 that FCM, R-FCM, ARKFCM and FCMRF algorithms are greatly affected by the bias field, and the MCR value gradually increases with the increase of the non-uniform intensity level. However, the MCR values of the MICO and NL-FCMRF algorithms hardly change with the change of the intensity inhomogeneity level, which shows that the two algorithms are little affected by the bias field, reflecting the robustness of the NL-FCMRF algorithm to the bias field of the images.

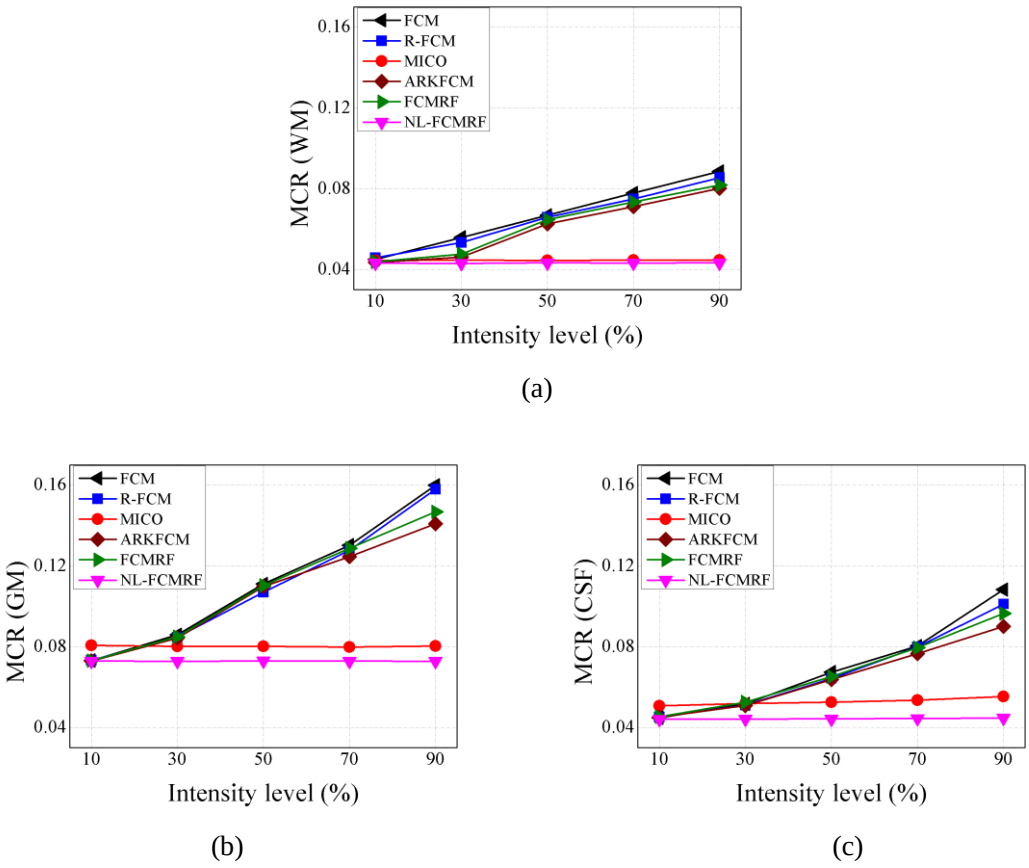


**Figure 5.** The variety curves of MCR values for brain MRI slices with different intensity level. (a) WM, (b) GM and (c) CSF.

4.1.3. Image segmentation with noise and intensity inhomogeneity

In the third experiment, the brain MRI images with noise and bias field are selected as the tested objects. These images are still sliced from the 3D brain MRI in three different directions: axial, sagittal and coronal, respectively, and they are corrupted by 70% intensity inhomogeneity and 7% noise level, as shown in the first row of Figure 6. The first column is the original brain MRI slice images, the second column is the ground truth, and the segmentation results of six algorithms (FCM, R-FCM, FCMRF, MICO, ARKFCM and NL-FCMRF) are shown in columns 3–8. By comparing the results, it can be seen that NL-FCMRF can still achieve better segmentation results.

Dice similarity coefficient (DSC) is often used to objectively evaluate different segmentation algorithms, which is defined as follows

$$\rho(S_1, S_2) = \frac{2|S_1 \cap S_2|}{|S_1| + |S_2|} \tag{31}$$

where $S_1$ and $S_2$ respectively denote the image segmented by the algorithm to be evaluated and ground truth, and $|\cdot|$ denotes the number of pixels after correlation operation. $\rho \in [0, 1]$, the greater the value of $\rho$, the better the segmentation performance. To compare segmentation results when the noise level varied from 3% to 33% for the MRI images with 100% intensity inhomogeneity level, we still tested 12 brain MRI slice images, extracted three brain tissues: WM, GM and CSF, and

compared the segmentation results of six algorithms. The experimental results are shown in Figure 7. It can be clearly seen from the changes of the data curve in Figure 7 that NL-FCMRF algorithm can effectively overcome the dual effects of noise and bias field, and the segmentation effect is the best compared with the other five algorithms.

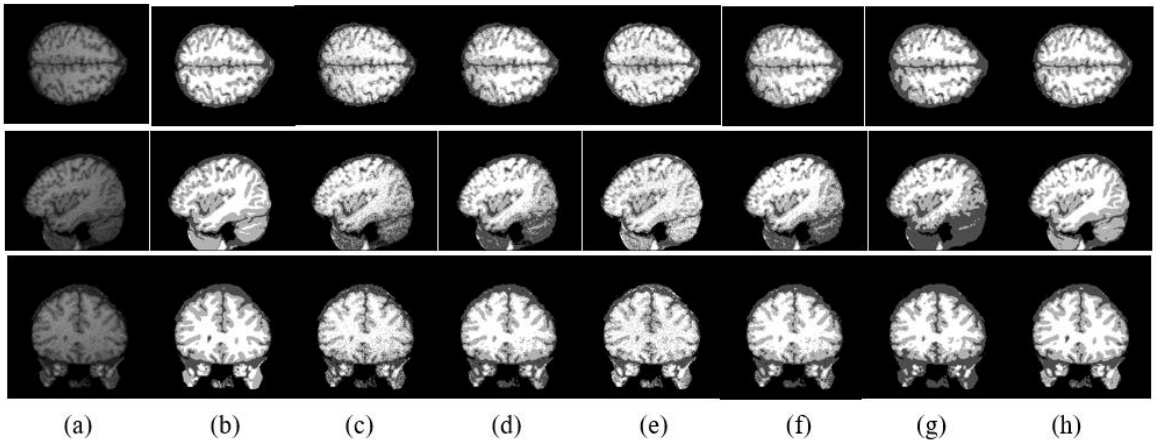


**Figure 6.** Segmentation results for MRI with intensity inhomogeneity and noise. (a) Brain MRI slice images, (b) ground truth, (c) FCM, (d) R-FCM, (e) MICO, (f) ARKFCM, (g) FCMRF and (h) NL-FCMRF.

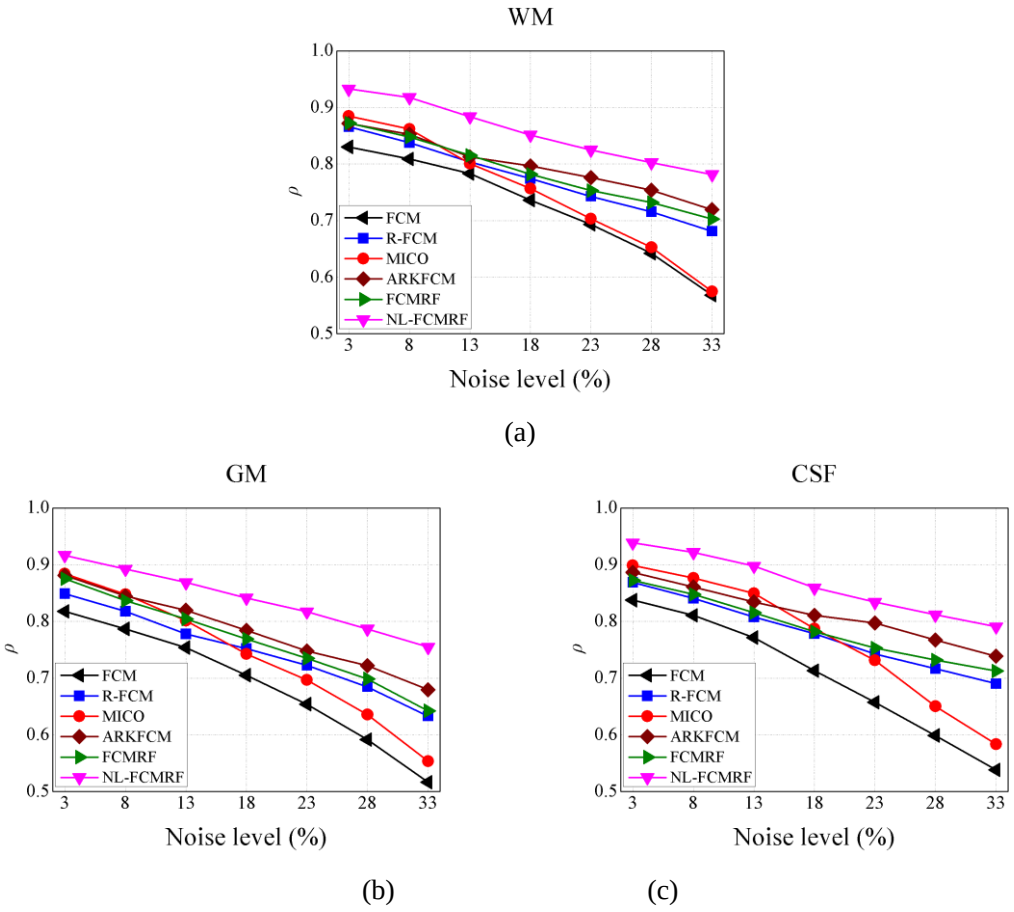


**Figure 7.** DSC comparison of three brain tissues segmentation results. (a) WM, (b) GM and (c) CSF.

*4.2. Results on real brain MRI image*

The real brain MRI images selected from the IBSR database [30] are used in this section. In the experiment, six MRI images with blurred boundaries and low contrast of brain tissue are used as experimental samples for segmentation testing, and the size of these images is 256 × 205 pixels.

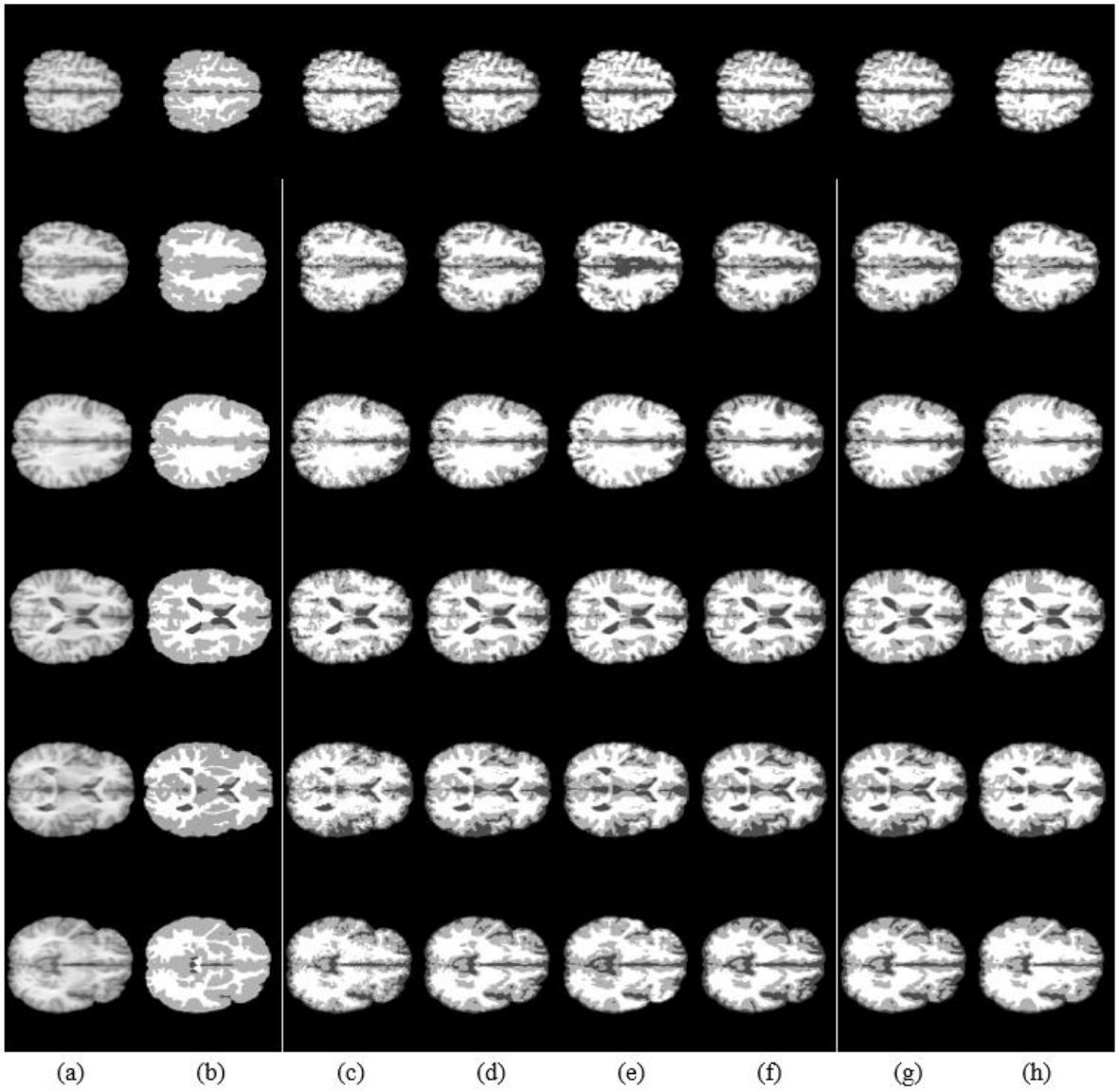


**Figure 8.** Segmentation results of real brain MRI. (a) Brain MRI slice images and their serial numbers are 125, 135, 145, 155, 165 and 175, (b) ground truth, (c)FCM, (d) R-FCM, (e) MICO, (f) ARKFCM, (g) FCMRF and (h) NL-FCMRF.

Six algorithms, FCM, R-FCM, MICO, ARKFCM, FCMRF and NL-FCMRF, are still used to process these images. The parameters of NL-FCMRF are the same as those in the previous section, and the experimental results are shown in Figure 8. Column 1 is six real brain MRI images with different slice numbers, there are intensity inhomogeneity and noise in these images. At the same time, the contrast between different brain tissues is low, and there is overlap blur at the edge. Column

2 is the ground truth, and columns 3-8 are the segmentation results of six algorithms. From the segmentation results, NL-FCMRF demonstrates a more accurate segmentation, which can overcome the problems of bias field, noise and low contrast in brain MRI. To further quantitatively compare and analyze the performance of the six algorithms, another objective evaluation index Jaccard coefficient (JS) shown in Eq (32) is used, and the experimental results are shown in Figure 9.

$$JS = \frac{|A_i \cap B_i|}{|A_i \cup B_i|} \tag{32}$$

where $A_i$ denotes the pixel set belonging to $i$-th cluster identified by the evaluated algorithm, while $B_i$ denotes the pixel set belonging to $i$-th cluster in the ground truth. As an index of similarity metric, the value of JS is bigger, the clustering performance is better, and vice versa. In Figure 9, the real brain MRI slices from three directions: axial, sagittal and coronal, respectively, and six algorithms in this paper are used to segment these slice images. The standard FCM has the worst robustness to noise. The ability against the noise of R-FCM and FCMRF is improved compared with FCM. However, R-FCM is not satisfactory at image edge and detail processing, and FCMRF is prone to over-segmentation. Compared with the above three algorithms, the robustness and detail preserve of NL-FCMRF have improved significantly. Next, the quantitative mean and standard deviation of the Jaccard coefficient is indicated for different direction slice images using six segmentation models, as shown in Table 2.

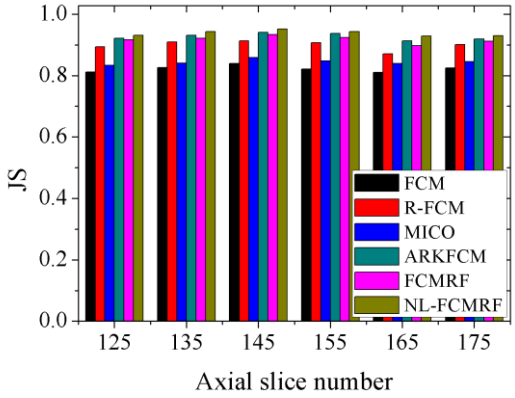


(a)

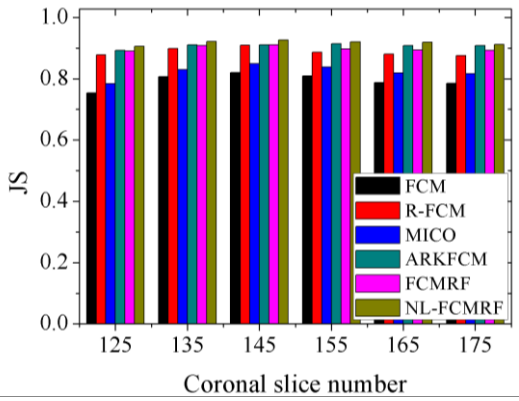


(b)

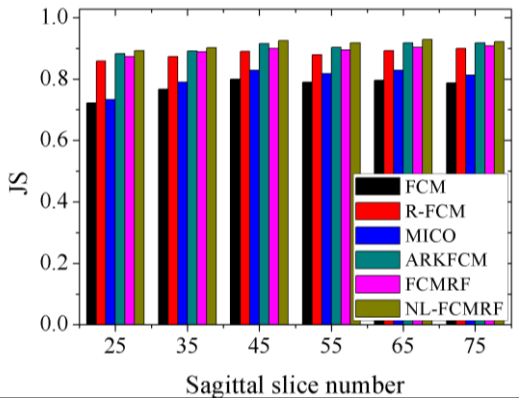


(c)

**Figure 9.** The comparison of segmentation results in axial, coronal and sagittal slices. (a) Comparison of JS values in the axial slice, (b) comparison of JS values in the coronal slice and (c) comparison of JS values in the sagittal slice.

**Table 2.** Mean and Standard Deviation of Jaccard Coefficient.

| Model | Axial slice | Coronal slice | Sagittal slice |
|---|---|---|---|
| FCM | 0.822±0.009 | 0.794±0.021 | 0.776±0.026 |
| R-FCM | 0.899±0.013 | 0.888±0.012 | 0.882±0.014 |
| MICO | 0.843±0.007 | 0.823±0.023 | 0.802±0.025 |
| ARKFCM | 0.927±0.010 | 0.907±0.019 | 0.904±0.021 |
| FCMRF | 0.917±0.011 | 0.898±0.008 | 0.895±0.012 |
| NL-FCMRF | 0.938±0.008 | 0.917±0.007 | 0.914±0.013 |

## 5. Conclusion

Using the mathematical and statistical model to describe the relationship between the local neighborhood pixels of an image can depict the structural features of the image more clearly. Therefore, a fuzzy c-means clustering model combined with Markov random field is proposed in this paper. This model defines a new distance measure incorporated with local statistical features to restrain the influence of low contrast and noise. At the same time, a non-local regular term is integrated into the energy function to improve the robustness of the algorithm to noise. In addition, the intensity inhomogeneity model is also introduced into the energy function to estimate the bias field. NL-FCMRF can effectively overcome the inherent defects in brain MRI, and its validity is proved in the segmentation experiments of simulated and real brain MRI images.

## Acknowledgment

This work is partially supported by Natural Science Foundation of Fujian Province (Grant No. 2020J01816, 2020J05169), the Principal Foundation of Minnan Normal University (Grant No. KJ18010), 2020 research project of the 13th Five-Year Plan of Educational Science in Fujian Province (Grant No. FJJKCG20-315) and 2021 undergraduate innovation and entrepreneurship training project in Fujian Province (Grant No. S202110402053).

## Conflict of interest

The authors have no conflict of interest.

## References

1. P. Moeskops, M. A.Viergever, A. M. Mendrik, L. S. De Vries, M. J. Benders, I. Isgum, Automatic segmentation of MR brain images with a Convolutional Neural Network, *IEEE Trans. Med. Imaging*, **35** (2016), 1252–1261. doi: 10.1109/TMI.2016.2548501.
2. A. Makropoulos, S. J. Counsell, D. Rueckert, A review on automatic fetal and neonatal brain MRI segmentation, *NeuroImage*, **170** (2017), 231–248. doi: 10.1016/j.neuroimage.2017.06.074

3. Y. Yang, W. Jia, Y. Yang, Multi-atlas segmentation and correction model with level set formulation for 3D brain MR images, *Pattern Recogn.*, **90** (2019), 450–463. doi: 10.1016/j.patcog. 2019.01.031
4. J. Song, Z. Zhang, Magnetic resonance imaging segmentation via weighted level set model based on local kernel metric and spatial constraint, *Entropy*, **23** (2021), 1196. doi: 10.3390/e23091196
5. L. Sun, L. Zhang, D. Zhang, Multi-Atlas based methods in brain MR image segmentation, *Chin. Med. Sci. J.*, **34** (2019), 110–119. doi: 10.24920/003576
6. J. Song, Z. Zhang, A modified robust FCM model with spatial constraints for brain MR image segmentation, *Information*, **10** (2019), 74. doi: 10.3390/info10020074
7. Z. Zhang, J. Song, An adaptive fuzzy level set Model with local spatial information for medical image segmentation and bias correction, *IEEE Access*, **7** (2019), 27322–27338. doi: 10.1109/ACCESS.2019.2900089
8. S. Roy, P. Maji, Medical image segmentation by partitioning spatially constrained fuzzy approximation spaces, *IEEE Trans. Fuzzy Syst.*, **28** (2020), 965–977. doi: 10.1109/TFUZZ.2020. 2965896
9. D. L. Pham, Spatial models for fuzzy clustering, *Comput. Vis. Image Und.*, **84** (2001), 285–297, doi: 10.1006/cviu.2001.0951.
10. W. Cui, Y. Wang, Y. Fan, Y. Feng, T. Lei, Localized FCM clustering with spatial information for medical image segmentation and bias field estimation, *J. BiomMed. Imaging*, **2013** (2013), 930301. doi: 10.1155/2013/930301
11. A. Jaiswal, M. A. Williams, A. Bhalerao, M. K. Tiwari, J. M. Warnett, Markov random field segmentation for industrial computed tomography with metal artefacts, *J. X-Ray Sci. Technol.*, **26** (2018), 573–591. doi: 10.3233/XST-17322
12. H. Liu, G. Dai, F. Pu, Hip-Joint CT image segmentation based on hidden Markov model with gauss regression constraints, *J. Med. Syst.*, **43** (2019), 309. doi: 10.1007/s10916-019-1439-6
13. X. Xu, Y. Guan, H. Gong, Z. Feng, Q. Luo, Automated brain region segmentation for single cell resolution histological images based on markov random Field, *Neuroinformatics*, **18** (2020), 181–197. doi: 10.1007/s12021-019-09432-z
14. A. Chen, Y. Zhang, Image segmentation based on a robust fuzzy c means algorithm, *J. Med. Imag. Health In.*, **9** (2019),1464–1468. doi: 10.1166/jmihi.2019.2745
15. J. Besag, Spatial interaction and the statistical analysis of lattice systems, *J. Royal Stat. Soc.*, **36** (1974), 192–236. https://www.jstor.org/stable/2984812
16. C. Sutton, A. Mccallum, An introduction to conditional random fields, *Found. Trends*, **4** (2012), 267–373. doi: 10.1561/2200000013
17. H. Rue, H. Tjelmeland, Fitting Gaussian Markov random fields to Gaussian fields, *Scand. J. Stat.*, **29** (2002), 31–49. doi: 10.1111/1467-9469.00058
18. F. Wu, The Potts model, *Rev. Mod. Phys.*, **54** (1982), 235–268. doi: 10.1103/RevModPhys.54. 235
19. S. Ribes, D. Didierlaurent, N. Decoster, E. Gonneau, L. Risser, V. Feillel, Automatic segmentation of breast MR images through a Markov random field statistical model, *IEEE Trans. Med. Imaging*, **33** (2014), 1986–1996. doi: 10.1109/TMI.2014.2329019
20. R. C. Dubes, A. K. Jain, Clustering techniques: The user's dilemma, *Pattern Recogn.*, **8** (1976), 247–260. doi: 10.1016/0031-3203(76)90045-5

21. J. C. Bezdek, Pattern recognition with fuzzy objective function Algorithms, *Adv. Appl. Pattern Recogn.*, **22** (1981), 203–239. doi: 10.1007/978-1-4757-0450-1
22. B. N. Subudhi, F. Bovolo, A. Ghosh, L. Bruzzone, Spatio-contextual fuzzy clustering with Markov random field model for change detection in remotely sensed images, *Opt. Laser Technol.*, **57** (2014), 284–292. doi: 10.1016/j.optlastec.2013.10.003
23. T. K. Palani, B. Parvathavarthini, K. Chitra, Segmentation of brain regions by integrating meta heuristic multilevel threshold with Markov random field, *Current Med. Imaging Rev.*, **12** (2016), 4–12. doi: 10.2174/1573394711666150827203434
24. O. Salih, S. Viriri, Skin lesion segmentation using Sto-chastic region-merging and pixel-based Markov random field, *Symmetry*, **12** (2020), 1224. doi: 10.3390/sym12081224
25. M. Hao, M. Zhou, J. Jin, W. Shi, An advanced superpixel-based Markov random field model for unsupervised change detection, *IEEE Geosci. Remote S.*, **17** (2020), 1401–1405. doi: 10.1109/LGRS.2019.2948660
26. X. Li, J. Chen, L. Zhao, S. Guo, X. Zhao, Adaptive distance-weighted Voronoi tessellation for remote sensing image segmentation, *Remote Sens.*, **12** (2020), 4115. doi:10.3390/rs12244115
27. J. Song, Z. Zhang, Brain tissue segmentation and bias field correction of MR image based on spatially coherent FCM with nonlocal constraints, *Comput. Math. Method Med.*, **2019** (2019), 4762490. doi: 10.1155/2019/4762490
28. Y. Chen, J. Li, H. Zhang, Y. Zheng, B. Jeon, Q. J. Wu, Non-local-based spatially constrained hierarchical fuzzy C-means method for brain magnetic resonance imaging segmentation, *Iet Image Process.*, **10** (2016), 865–876. doi: 10.1049/iet-ipr.2016.0271
29. BrainWeb: Simulated Brain Database, Available online: http://brainweb.bic.mni.mcgill.ca/brainweb/. (accessed on 28 August 2021).
30. IBSR: The Internet Brain Segmentation Repository, Available online: http://www.nitrc.org/projects/ibsr. (accessed on 29 August 2021)
31. C. Li, J. Gore, C. Davatzikos, Multiplicative intrinsic component optimization (MICO) for MRI bias field estimation and tissue segmentation, *Magn. Reson. Imaging*, **32** (2014), 913–923. doi: 10.1016/j.mri.2014.03.010
32. A. Elazab, C. Wang, F. Jia, Q. Hu, Segmentation of brain tissues from magnetic resonance images using adaptively regularized kernel-based fuzzy c-means clustering, *Comput. Math. Method. M.*, **2015** (2015), 485495. doi: 10.1155/2015/485495
33. S. Zhan, X. Yang, MR image bias field harmonic approximation with histogram statistical analysis, *Pattern Recogn. Lett.*, **83** (2016), 91–98. doi: 10.1016/j.patrec.2016.02.009